# Giant DC-like residual current generated by subcycle laser pulses

Adrian Seith, Ferdinand Evers, and Jan Wilhelm*
*Institute of Theoretical Physics and Regensburg Center for Ultrafast Nanoscopy (RUN), University of Regensburg, D-93053 Regensburg, Germany*

(Received 2 February 2024; accepted 24 September 2024; published 18 November 2024)

Experimental indications have been reported suggesting that laser pulses shining on materials with relativistic dispersion can produce currents that survive long after the illumination has died out. Such residual currents, i.e., remnant currents, have applications in petahertz logical gates. The remnant currents' strength strongly depends on the pulse shape. We develop an analytical formula that allows one to optimize the pulse shape for remnant current production; we predict remnant currents exceeding the values observed so far by up to five orders of magnitude. This can be achieved by using single-cycle pulses instead of the previously employed multicycle pulses. In fact, remnant currents can be almost as strong as the peak current under irradiation.

DOI: 10.1103/PhysRevResearch.6.043149

## I. INTRODUCTION

The dynamics of currents induced by an ultrashort laser pulse in a metal or semiconductor is strongly influenced by the pulse's shape and amplitude. Improvements in pulse-shape engineering [1–6] have provided access to a plethora of phenomena on subcycle timescales. Such phenomena include the generation of high harmonics [2,7–15], dynamical Bloch oscillations [2,16,17], and ultrafast clocking of electron-electron correlations [18]. With an eye on applications, it has been proposed that pulse-shape engineering and the associated control of microscopic currents should be viewed as a prerequisite of ultrafast light-wave electronics [1,19–31]. In this context, experimental observations are of relevance, reporting that suitable pumping pulses can produce a DC- like residual or remnant current [19,32,33], which persists long after the pumping pulse, whose duration typically is of the order of 10 to 100 fs, has died out. Experiments show a strong dependence of remnant currents on the pulse shape and, in particular, on its carrier-envelope phase (CEP) [34,35], in agreement with density matrix simulations [36]. As a corresponding application, a petahertz logic gate [37] has been proposed.

In order to use remnant currents as an efficient tool for light-wave driven electronics, the remnant amplitude per incoming laser pulse should be maximized, for instance, to reduce energy consumption. Given many pulse-shape parameters—amplitude, carrier frequency, carrier-envelope phase, pulse duration, etc.—and additional material parameters, it is not straightforward to find an optimal setup to produce large-amplitude remnant currents. Pulse-shape optimization is most conveniently achieved if analytical expressions are known that reflect transparent parametric dependencies. While the commonly used semiclassical approximation to density matrix dynamics yields analytic formulas, it fails to explain the phenomenon of remnant currents [38]; a quantum mechanical analysis of the dynamics of noninteracting Bloch electrons is required, while light can be treated as a classical phenomenon.

In this work, we present an analysis that enables us to optimize parameters for finding large-amplitude remnant currents. A formula is derived from third-order perturbation theory to the time evolution mediated by the semiconductor Bloch equations (SBEs) [39–54]. In the limit of large effective damping, i.e., $\tilde{\omega} := \omega/\gamma < 1$, with $\omega$ being the carrier frequency and $\gamma$ being the dephasing rate of the coherences, it adopts a transparent form; the remnant current density $\mathbf{j}^{(\infty)}$ is given by

$$\mathbf{j}^{(\infty)} = CE_0^3 \mathcal{F}[s]\{\hat{\mathbf{e}}_\parallel[1+O(\tilde{\omega})] + \hat{\mathbf{e}}_\perp O(\tilde{\omega})\} + \hat{\mathbf{e}}_\parallel O\big(\tilde{E}_0^4\big) + \hat{\mathbf{e}}_\perp O\big(\tilde{E}_0^4\big), \tag{1}$$

where $C$ is a material-dependent constant, $\hat{\mathbf{e}}_\parallel$, $\hat{\mathbf{e}}_\perp$ with $\hat{\mathbf{e}}_\parallel \perp \hat{\mathbf{e}}_\perp$ denote unit vectors; $\tilde{E}_0 := q\sigma E_0/k_\mathrm{F}$ is the small parameter in the perturbative expansion, with $q$ denoting the electron charge, $k_\mathrm{F}$ the Fermi vector as a typical length scale, $\sigma$ the duration, and $E_0$ the amplitude of the linearly polarized transient electric field,

$$\mathbf{E}(t) := E(t)\,\hat{\mathbf{e}}_\parallel := E_0\, s(t)\,\hat{\mathbf{e}}_\parallel. \tag{2}$$

The functional $\mathcal{F}[s]$ in (1) depends on the pulse shape $s(t)$, $\max|s(t)| = 1$; examples of $s(t)$ are sketched in Figs. 1(a) and 1(b). We show that the value of $\mathcal{F}[s]$ strongly depends on $s(t)$; in particular, $\mathbf{j}^{(\infty)}$ can be three orders of magnitude larger for single-cycle pulses [4,5] [Fig. 1(b)] compared to multicycle pulses [Fig. 1(a)] that have previously been used for generating remnant currents in experiments [34–37]. We predict that the use of single-cycle pulses [4,5] will result in remnant currents that are almost as strong as the transient currents during illumination. We also show that the material

*Contact author: jan.wilhelm@physik.uni-regensburg.de

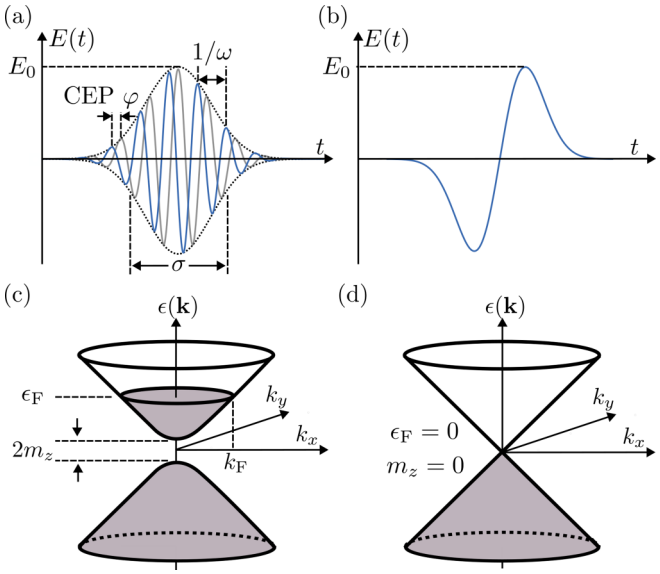


FIG. 1. Illustration of (a) pulse parameters and (c) material parameters that influence remnant currents. (b) and (d) show optimal parameters for producing large remnant currents. (a) Relevant pulse parameters to model experimental pulses in ultrafast dynamics [[2,4–6,15,19,33–35],[37,52,55,56]]: amplitude $E_0$, frequency $\omega$, CEP $\varphi$, pulse length $\sigma$. (b) The single-cycle limit of these pulses with $\varphi = 0$ leading to the largest remnant currents. (c) Material parameters of Dirac fermions: gap $m_z$, Fermi vector $k_F$, and Fermi level $\epsilon_F$, related to the Fermi velocity $v_F = \epsilon_F/k_F$. (d) The limit of gapless Dirac fermions, $m_z = 0$, at half filling, $\epsilon_F = 0$, produces the largest remnants.

constant $C$ strongly depends on the band structure; $C$ is larger for a gapless Dirac cone [Fig. 1(d)] compared to a massive Dirac cone [Fig. 1(c)]. We also show that Eq. (1) for remnant currents gives semiquantitative predictions in the case of large field strength and weak damping, $\omega/\gamma > 1$.

This manuscript is organized as follows: Section II introduces the SBE formalism to calculate remnant currents. Section III provides a numerical illustration of remnant currents computed from SBEs. In Sec. IV, we derive the analytical expression for remnant currents, given by Eq. (1), which is then applied in Sec. V to optimize pulse shapes and in Sec. VI to discuss materials, in order to obtain large remnant currents.

## II. SBE FORMALISM FOR CALCULATING TIME-DEPENDENT CURRENTS

To describe the dynamics of noninteracting Bloch electrons, we employ the density-matrix-based SBE formalism [11,39,41–54]. In the velocity gauge, the SBEs are given by

$$\left[\mathrm{i}\frac{\partial}{\partial t} + \mathrm{i}(1-\delta_{nn'})\gamma - \epsilon_{nn'}(\mathbf{k}_t)\right]\varrho_{nn'}(\mathbf{k},t) = \mathbf{E}(t)\sum_{\underline{n}}\varrho_{n\underline{n}}(\mathbf{k},t)\mathbf{d}_{\underline{n}n'}(\mathbf{k}_t) - \mathbf{d}_{n\underline{n}}(\mathbf{k}_t)\varrho_{\underline{n}n'}(\mathbf{k},t), \quad (3)$$

adopting the nomenclature from Ref. [52]: The lattice-periodic part of the Bloch eigenstates $|n\mathbf{k}\rangle$ solves the eigenvalue equation of the initial (unperturbed) Bloch Hamiltonian, $h(\mathbf{k})\,|n\mathbf{k}\rangle = \epsilon_n(\mathbf{k})\,|n\mathbf{k}\rangle$. The crystal momentum has a time dependence stemming from minimal coupling,

$$\mathbf{k}_t := \mathbf{k} - \mathbf{A}(t), \quad \mathbf{A}(t) := -q\int_{t_0}^{t}\mathbf{E}(t')\mathrm{d}t', \quad (4)$$

where $\mathbf{A}(t)$ can be interpreted as a vector potential. $\epsilon_{n\underline{n}}(\mathbf{k}_t) := \epsilon_n(\mathbf{k}_t) - \epsilon_{\underline{n}}(\mathbf{k}_t)$ is the energy difference of two bands $n, \underline{n}$ at crystal momentum $\mathbf{k}_t$ in the Brillouin zone (BZ) and $\mathbf{d}_{n\underline{n}}(\mathbf{k}_t) = q\langle n\mathbf{k}_t|\mathrm{i}\partial_{\mathbf{k}_t}|\underline{n}\mathbf{k}_t\rangle$ is the transition dipole matrix element coupling to the electric driving field $\mathbf{E}(t)$. $\varrho_{nn'}(\mathbf{k},t) := \langle n\mathbf{k}_t|\hat{\rho}|n'\mathbf{k}_t\rangle$ are the matrix elements of the density operator $\hat{\rho}$. The diagonal elements of the density matrix describe the occupation $f_n(\mathbf{k}_t,t)$ of the $n$th band at $\mathbf{k}_t$ in the BZ. In the rest of the manuscript, we will use the following notation:

$$f_n(\mathbf{k}_t,t) = \varrho_{nn}(\mathbf{k},t). \quad (5)$$

Off-diagonal elements of the density matrix describe the ability of the system to maintain coherent superposition between two states and thus are called coherences.

Many-body interactions, such as electron-electron or electron-phonon scattering, lead to dephasing in electron dynamics [42,54,57–59]. In the context of Eq. (3), dephasing dampens the off-diagonal density matrix elements $\varrho_{nn'}(\mathbf{k},t), n \neq n'$ towards zero. This damping is traditionally modeled by phenomenological dephasing rates, $\gamma_{n,n'}(\mathbf{k})$ [57,59–62], which here we take as independent of $\mathbf{k}$ and the band indices: $\gamma_{nn'}(\mathbf{k}) := \gamma = 1/T_2$ with $n \neq n'$ and $T_2$ is the dephasing time. The typical values for $T_2$ used in the literature range from 1 to 100 fs [9,10,16,37,58,59,61–64]. The overall value is surprisingly short, partially on the scale of the fastest intrinsic processes. Therefore, it has been argued that in addition to dephasing, $\gamma$ could also account for an incoherent average over different sample regions [58]. The relaxation of occupation numbers $f_n(\mathbf{k}_t,t)$ towards the ground-state occupation $f_n^{(0)}(\mathbf{k})$ requires reshuffling of energy and, for this reason, inelastic scattering processes. Therefore, the related timescale $T_1$ differs from the dephasing time, typically, $T_2 \ll T_1$. For topological surface states, $T_1$ exceeds a picosecond [20,65], and thus is even significantly longer than the experimental pulse durations. Thus motivated, we will assume a vanishing relaxation rate $T_1^{-1} = 0$ in our calculations.

In this limit, the remnant current is given by

$$\mathbf{j}^{(\infty)} := \lim_{t\to\infty} q\sum_n \int_{\mathrm{BZ}} \frac{\mathrm{d}\mathbf{k}}{(2\pi)^d}\,\partial_{\mathbf{k}_t}\epsilon_n(\mathbf{k}_t)f_n(\mathbf{k}_t,t), \quad (6)$$

where the limit of large times is characterized by the times exceeding the pulse duration, $t \gg \sigma$ and $\gamma t \gg 1$. In the case of inversion symmetry and/or time-reversal invariance, the energy derivative in the integrand is odd in $\mathbf{k}$. Correspondingly, nonzero remnant currents arise from the odd components of the final population $\lim_{t\to\infty} f_n(\mathbf{k}_t,t)$.

## III. NUMERICAL ILLUSTRATION OF REMNANT CURRENTS

Before we sketch the analytical derivation, we present a numerical simulation to illustrate remnant currents in a driven

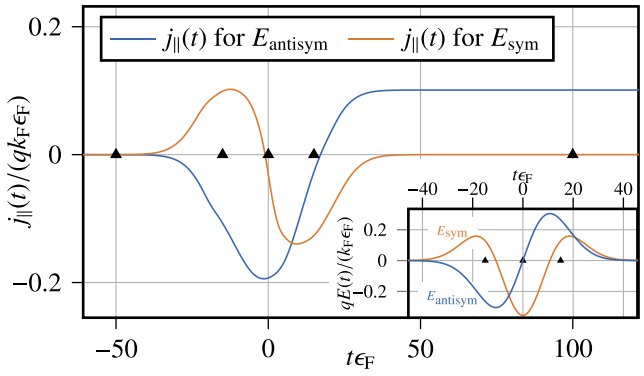


FIG. 2. Current density $j_\parallel(t)$ along the direction of the electric field in a gapless Dirac band structure. The plot shows a residual current $j_\parallel^{(\infty)}$ that strongly depends on the incoming pulse shape: single node ($E_{\text{antisym}}$) vs double node ($E_{\text{sym}}$). As shown, remnant currents can be of the same order of magnitude as the transient current. Triangles mark the times at which the occupations in Fig. 3 are evaluated. Inset: Electric field pulse from Eq. (19) with field amplitude $E_0 = 0.5$ MV/cm and pulse duration $\sigma = 50$ fs leading to a carrier frequency of ≈6.4 THz. The Hamiltonian parameters are chosen as typical values for a topological surface state [12,52]: Fermi velocity $v_F = 0.43$ nm/fs, Fermi energy $\epsilon_F = 0.2$ eV above the minimum of the conduction band, vanishing mass $m_z = 0$, implying a timescale $\epsilon_F^{-1} = 3.3$ fs and a scale for the electric field amplitude $k_F\epsilon_F/q = 1.41$ MV/cm. The dephasing time is $T_2 = 1/\gamma = 10$ fs.

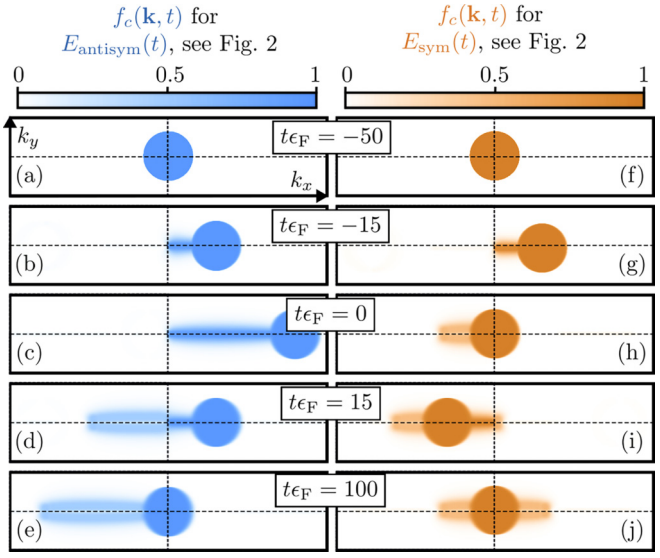


FIG. 3. Time-dependent occupation of the conduction band $f_c(\mathbf{k},t)$ of the gapless Dirac cone driven by the two pulses shown in the inset of Fig. 2. Occupations of the antisymmetric pulse (blue) are shown in (a)–(e) at different times; the final occupation (e) is asymmetric, leading to a large remnant current. Occupations of the symmetric pulse (orange) are shown in (f)–(j) at different times; the final occupation (j) is symmetric, suppressing the remnant current. Time points are marked by triangles in Fig. 2.

Dirac system with Hamiltonian

$$h(\mathbf{k}) := v_F(k_x\sigma_y - k_y\sigma_x) + m_z\sigma_z, \tag{7}$$

where $v_F$ is the Fermi velocity and $m_z$ is the mass parameter. This model has been frequently employed to describe the low-energy excitations of graphene [66], two-dimensional semiconductors [67], and topological surface states [68]. For computing remnant currents, we solve the SBE, given by Eq. (3), on a discretized mesh approximating the Brillouin zone using a fourth-order Runge-Kutta solver with discrete time steps. Information about numerical convergence checks can be found in Appendix D. For a detailed derivation and information about the implementation of the SBE, we refer to [52].

Figure 2 displays the current density parallel to the electric field for a gapless Dirac cone, $m_z = 0$, with $E(t)$ defined in the inset; the perpendicular current vanishes [69]. As seen there, the remnant current in the direction of the driving field, $j_\parallel^{(\infty)} := \mathbf{j}^{(\infty)} \cdot \hat{\mathbf{e}}_\parallel$, reaches the same magnitude as the peak of $|j_\parallel(t)|$ and is, in this sense, gigantic. As we show in the following, using single-cycle pulses with a CEP leading to a suitable nodal structure is key to producing giant remnant currents.

To further illustrate how remnant currents arise, in Fig. 3, we show the time-dependent conduction band occupation $f_c(\mathbf{k},t)$ as a response to the pulses given in Fig. 2. The interplay of Bloch acceleration of electrons via Eq. (4) and interband excitations leads to residual population differences at $t \to \infty$; see Fig. 3. For the antisymmetric pulse (blue trace of Fig. 2), the residual population is displayed in Fig. 3(e). It shows a large asymmetry with respect to the $k_y$ axis, which, via Eq. (6), is leading to the giant residual currents for the blue trace in Fig. 2. In contrast, the symmetric pulse (orange trace of Fig. 2) leads to the symmetric distribution of occupations in Fig. 3(f) and, hence, zero residual currents. We briefly discuss the effect of a finite $T_1$ time. Introducing a nonvanishing damping rate $T_1^{-1}$ on the diagonal elements of the density matrix implies the relaxation of the occupation numbers to their equilibrium values at $t \gg T_1$ and, hence, remnant currents decay exponentially at longest times.

## IV. POWER EXPANSION OF THE SBE

For the analysis of remnant currents as a function of pulse shape and material parameters, we expand the time-dependent density matrix $\varrho(t)$ in a dimensionless parameter proportional to the electric field strength $E_0$.

Straightforwardly, the leading term in this expansion is of third order or higher in $E_0$: remnant current amplitudes cannot be linear in the driving field. This is because in linear response $\mathbf{j}(t) = \int_{-\infty}^{t} \sigma(t-t')\mathbf{E}(t')\mathrm{d}t'$, the integral is dominated by times $t \sim t'$ because of the limited memory of the conductivity $\sigma$. Specifically, $\mathbf{j}$ vanishes at times $t$ so large that the peak time of $\mathbf{E}(t)$ has passed by more than the memory time. Further, for the inversion or time-reversal symmetric models that we have in mind, remnant currents flip their sign if $E(t)$ does, and therefore even-order terms in $E_0$ cannot arise [70].

The derivation of the analytical expression of remnant currents, given by Eq. (1), starts with a matrix-vector formulation of the SBE (3): Writing the density matrix as a vector $\boldsymbol{\varrho}(\mathbf{k},t) = [\varrho_{nn'}(\mathbf{k},t)]_{nn'}$, with the double index $nn'$ as

the vector index, we have

$$\mathrm{i}\frac{\partial}{\partial t}\boldsymbol{\varrho}(\mathbf{k},t) = (\mathbb{h}(\mathbf{k}_t) + \mathbb{V}(\mathbf{k}_t,t))\boldsymbol{\varrho}(\mathbf{k},t), \tag{8}$$

with matrices $\mathbb{h}$ and $\mathbb{V}$ defined via their matrix elements,

$$\begin{aligned} h_{nn',mm'} &:= \delta_{nm}\delta_{n'm'}[\epsilon_{nn'}(\mathbf{k}_t) - \mathrm{i}\gamma], \\ V_{nn',mm'} &:= \mathbf{E}(t)[\delta_{nm}\mathbf{d}_{m'n'}(\mathbf{k}_t) - \delta_{n'm'}\mathbf{d}_{nm}(\mathbf{k}_t)]. \end{aligned} \tag{9}$$

To perform a perturbative expansion in $\mathbb{V}$, we transform Eq. (8) into the interaction picture,

$$\mathrm{i}\frac{\partial}{\partial t}\boldsymbol{\varrho}_I(\mathbf{k},t) = \mathbb{V}_I(\mathbf{k}_t,t)\boldsymbol{\varrho}_I(\mathbf{k},t), \tag{10}$$

with

$$\begin{aligned} \boldsymbol{\varrho}_I(\mathbf{k},t) &:= e^{\mathrm{i}\int_{t_0}^{t}\mathbb{h}(\mathbf{k}_{t'})\mathrm{d}t'}\boldsymbol{\varrho}(\mathbf{k},t), \\ \mathbb{V}_I(\mathbf{k}_t,t) &:= e^{\mathrm{i}\int_{t_0}^{t}\mathbb{h}(\mathbf{k}_{t'})\mathrm{d}t'}\mathbb{V}(\mathbf{k}_t,t)e^{-\mathrm{i}\int_{t_0}^{t}\mathbb{h}(\mathbf{k}_{t'})\mathrm{d}t'}. \end{aligned} \tag{11}$$

Here, we can neglect the time-ordering operator because $[\mathbb{h}(\mathbf{k}_t), \mathbb{h}(\mathbf{k}_{t'})] = 0$. The initial condition of the system is given by $\varrho^{(0)}_{I,ij}(\mathbf{k}) = \varrho_{ij}(\mathbf{k},t_0)\delta_{ij} = f^{(0)}_i(\mathbf{k})\delta_{ij}$. Time integration of Eq. (11) and iterative insertion of $\boldsymbol{\varrho}_I(\mathbf{k},t)$ leads to a series expansion in $\mathbb{V}_I$,

$$\begin{aligned} \boldsymbol{\varrho}_I(\mathbf{k},t) = \boldsymbol{\varrho}^{(0)}(\mathbf{k}) &+ \frac{1}{\mathrm{i}}\int_{t_0}^{t}\mathrm{d}t_1\mathbb{V}_I(\mathbf{k}_{t_1},t_1)\boldsymbol{\varrho}^{(0)}(\mathbf{k}) \\ &- \int_{t_0}^{t}\mathrm{d}t_1\int_{t_0}^{t_1}\mathrm{d}t_2\mathbb{V}_I(\mathbf{k}_{t_1},t_1)\mathbb{V}_I(\mathbf{k}_{t_2},t_2)\boldsymbol{\varrho}^{(0)}(\mathbf{k}) + \cdots . \end{aligned} \tag{12}$$

Inserting Eq. (11) into Eq. (12), we observe that linear terms in $\mathbb{V}$ do not change the occupations $f_n(\mathbf{k}_t,t)$; including second-order terms, given by Eq. (12), implies

$$\begin{aligned} f_n(\mathbf{k}_t,t) = f^{(0)}_n(\mathbf{k}) &+ \sum_{\underline{n}}\left[f^{(0)}_{\underline{n}}(\mathbf{k}) - f^{(0)}_n(\mathbf{k})\right] \\ &\times \int_{t_0}^{t}\mathrm{d}t_1\int_{t_0}^{t_1}\mathrm{d}t_2\Big[e^{[t_2\gamma+\mathrm{i}w_{n\underline{n}}(t_2)]-[t_1\gamma+\mathrm{i}w_{n\underline{n}}(t_1)]} \\ &\times \mathbf{E}(t_1)\cdot\mathbf{d}_{\underline{n}n}(\mathbf{k}_{t_1})\mathbf{E}(t_2)\cdot\mathbf{d}_{n\underline{n}}(\mathbf{k}_{t_2}) + \mathrm{c.c.}\Big] + O\big\{[\sigma\mathbf{E}\cdot\mathbf{d}(\mathbf{k}_t)]^3\big\}, \end{aligned} \tag{13}$$

with $w_{n\underline{n}}(t) := \int_{t_0}^{t}\epsilon_{n\underline{n}}(\mathbf{k}_{t'})\,\mathrm{d}t'$ the integral of the $\mathbf{k}_t$-dependent gap, $\mathbf{E}\cdot\mathbf{d}(\mathbf{k}_t)$ the dipole coupling, and $\sigma$ the pulse duration appearing in Eq. (13) due to the time integrals in the perturbative expansion. In particular, the occupation of the $n$th band $f_n(\mathbf{k}_t,t)$ changes as soon as $[f^{(0)}_n(\mathbf{k}) - f^{(0)}_{\underline{n}}(\mathbf{k})]$ is nonvanishing.

Similar expansions of SBEs have already been employed earlier to calculate higher-order responses to continuous driving [41,71–73]. This power-law expansion, however, only holds true if the perturbation $\sigma\mathbf{E}\cdot\mathbf{d}(\mathbf{k}_t)$ can be assumed to be small. This leads to the constraint on the Hamiltonian, where the dipole moments need to be free of any divergence or divergent terms have to be excluded in the BZ integral of Eq. (6), for example, by choosing a nonzero Fermi energy $\epsilon_\mathrm{F}$.

We considerthe Markov regime with fast damping compared to the typical rate of change of the electric field, i.e., $\tilde{\omega} = \omega/\gamma \ll 1$ if the rate of change is characterized mainly by a single frequency $\omega$. For the series of integrals, such as displayed in Eq. (13), the Markov limit implies that all times prior to $t_1$ will be replaced by $t_1$ in the integrand. The remaining integrals can be performed analytically, where each time integration produces a prefactor of the order of $\tilde{\omega}$, so that $\delta f^{(l)}/\delta f^{(2)} \propto \tilde{\omega}^{l-2}$ for orders $l = 3$ or higher. Hence, terms of order three or higher in the dipole coupling are subleading in the Markov limit and will be ignored. The remaining terms are

$$\begin{aligned} f_n(\mathbf{k}_t,t) = f^{(0)}_n(\mathbf{k}) &+ \sum_{\underline{n}}\left[f^{(0)}_{\underline{n}}(\mathbf{k}) - f^{(0)}_n(\mathbf{k})\right] \\ &\times \int_{t_0}^{t}\mathrm{d}t_1\frac{2\left|E(t_1)d^{\parallel}_{n\underline{n}}(\mathbf{k}_{t_1})\right|^2}{\gamma\left[1+\tilde{\epsilon}^2_{n\underline{n}}(\mathbf{k}_{t_1})\right]}[1+O(\tilde{\omega})] \\ &+ O\{[\sigma\mathbf{E}\cdot\mathbf{d}(\mathbf{k}_t)]^3\}, \end{aligned} \tag{14}$$

where $\tilde{\epsilon} := \epsilon/\gamma$ and $d^{\parallel}_{n\underline{n}}(\mathbf{k}) := \hat{\mathbf{e}}_{\parallel}\cdot\mathbf{d}_{n\underline{n}}(\mathbf{k})$. Further details about the Markov regime can be found in Appendix B.

The driving field strength $E_0$ enters the occupation dynamics, given by Eq. (14), explicitly in the numerator of the integrand; it also enters in the argument $\mathbf{k}_t = \mathbf{k} - \mathbf{A}(t)$, where it manifests in terms of order higher than two. The small dimensionless parameter in the expansion of $\mathbf{k}_t$ is $\tilde{E}_0 := E_0 q\sigma/k_\mathrm{F}$, where the charge $q$ and the pulse duration $\sigma$ enter due to the definition of $\mathbf{A}(t)$ in Eq. (4) and the Fermi vector $k_\mathrm{F}$ due to the $\mathbf{k}$ derivative. In the presence of inversion or time-reversal symmetry, the contribution of the order of $E_0^2$ in $f_n$ is an even function and therefore the remnant current corresponding to this order vanishes, as expected. A similar symmetry argument can be used to see that all third-order contributions proportional to $[\sigma\mathbf{E}\cdot\mathbf{d}(\mathbf{k})]^3$ and contributions up to cubic order in $\tilde{E}_0$ to remnant currents orthogonal to the driving field vanish.

In summary, the surviving terms in the Markov limit lead to Eq. (1), where the material constant is defined as

$$\begin{aligned} C := 2q^2\int_{\mathrm{BZ}}\frac{\mathrm{d}\mathbf{k}}{(2\pi)^d}\sum_{n\underline{n}}&\left[f^{(0)}_{\underline{n}}(\mathbf{k}) - f^{(0)}_n(\mathbf{k})\right] \\ &\times\frac{[\partial_{k_\parallel}\tilde{\epsilon}_n(\mathbf{k})]}{1+\tilde{\epsilon}^2_{n\underline{n}}(\mathbf{k})}\left[\partial_{k_\parallel}\left|d^{\parallel}_{n\underline{n}}(\mathbf{k})\right|^2 - \left|d^{\parallel}_{n\underline{n}}(\mathbf{k})\right|^2\frac{\partial_{k_\parallel}\left|\tilde{\epsilon}_{n\underline{n}}(\mathbf{k})\right|^2}{1+\tilde{\epsilon}^2_{n\underline{n}}(\mathbf{k})}\right]; \end{aligned} \tag{15}$$

$\mathcal{F}[s]$ in Eq. (1) abbreviates the functional

$$\mathcal{F}[s] := \int_{t_0}^{\infty}\mathrm{d}t\,[s(t)]^2\int_{t_0}^{t}\mathrm{d}t'\,s(t'). \tag{16}$$

Equation (1) is an expression for remnant currents given as a double expansion in the field strength $E_0$ and the inverse effective dephasing $\tilde{\omega}$. For small field strengths and fast dephasing relative to the electric field oscillation $\gamma > \omega$, we identify, for the parallel current,

$$\hat{j}^{(\infty)}_{\parallel} = C\mathcal{F}[s]E_0^3, \tag{17}$$

as the leading contribution to the remnant currents.

We now discuss higher-order terms by comparing the analytics from Eq. (17) with numerically exact computations. By comparing the numerically exact data $j^{(\infty)}_{\parallel}$ with the leading

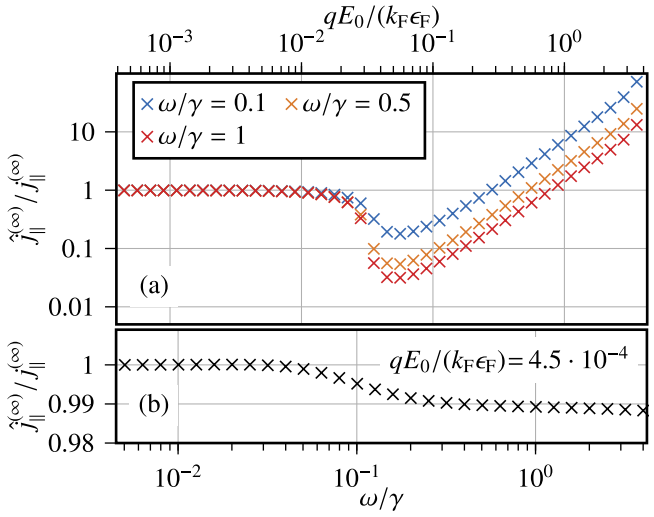


FIG. 4. Comparison of the analytical, leading-order result $\hat{j}_\parallel^{(\infty)}$ of the remnant current, given by Eq. (17), and numerically exact solutions $j_\parallel^{(\infty)}$ of Eq. (6) for a gapless Dirac system with Fermi energy $\epsilon_F/\gamma = 3$. (a) Ratio $\hat{j}_\parallel^{(\infty)}/j_\parallel^{(\infty)}$ as a function of the field strength $E_0$ for different dephasing rates $\omega/\gamma$. The evolution of this deviation with increasing damping times $\omega/\gamma$ is plotted in (b) at $E_0 = 4.5 \times 10^{-4} k_F\epsilon_F/q$, which is deep in the cubic regime; see (a). Simulation parameters are chosen as described in the caption of Fig. 2.

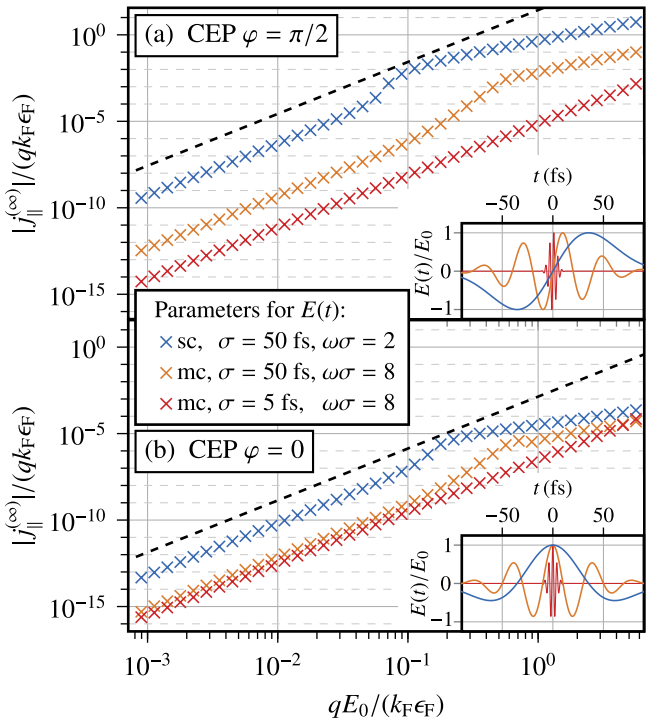


FIG. 5. Remnant current $j_\parallel^{(\infty)}$ computed from SBE for varying field strengths $E_0$ for pulses with CEP of (a) $\varphi = \pi/2$ and (b) $\varphi = 0$. Dashed lines are shown as a guide for the $E_0^3$ dependence. Inset: Shape of electric field pulses. We choose a Dirac Hamiltonian with parameters as described in the caption of Fig. 2. Blue traces correspond to a sc pulse according to Eq. (19); orange and red traces correspond to mc pulses according to Eq. (18).

contribution $\hat{j}_\parallel^{(\infty)}$, Fig. 4 confirms the cubic field strength dependence of remnant currents. As shown in Fig. 4(b), the deviation between $\hat{j}_\parallel^{(\infty)}$ and $j_\parallel^{(\infty)}$ in the small field strength limit is below 2% for all considered damping rates $0 < \omega/\gamma < 4$. Figure 4(a) also shows that starting at a certain field strength value, $qE_0/(k_F\epsilon_F) \approx 0.02$, higher-order terms start to influence remnant currents and the approximations made in the previous sections break down.

## V. OPTIMIZING PULSE SHAPES

*Analytics.* In the integrand in Eq. (16), we identify two factors: the first, $s(t)^2$, is non-negative. Further, the second factor, $\int_{t_0}^{t} dt' s(t') = -A(t)/(qE_0)$, represents an integral over a function $s(t')$ that can be interpreted as a normalized vector potential. It can exhibit nodes, i.e., sign changes; see the inset of Fig. 2. Depending on the nodal structure, the integrand can be positive (inset, blue trace) or oscillating (inset, orange trace); the latter implies partial cancellations in the main integral over the time $t$ in Eq. (16). To produce large remnant currents, pulse shapes with well-defined polarity of the vector potential $A(t)$ are preferential in order to avoid cancellations. The antisymmetrically shaped electric field (blue pulse in the inset of Fig. 2) corresponds to $A(t) < 0$ and represents a typical example.

In the following, we will apply Eqs. (1) and (16) for a systematic optimization of the pulse parameters with respect to remnant current production. A general model for pulse shapes considered in [[2,4–6,15,19,33–35],[37,52,55,56]] is

$$E(t) := E_0[\cos(\omega t + \varphi) + \alpha]\, e^{-(t/\sigma)^2}, \tag{18}$$

with parameters CEP $\varphi$ [74], frequency $\omega$, and width parameter $\sigma$ [75]. The factor $\alpha := -e^{-(\omega\sigma)^2/4}\cos(\varphi)$ is included to satisfy $\lim_{t\to\infty}\int_{-\infty}^{t} \mathbf{E}(t')dt' = 0$, which ensures gauge consistency. In the limit $\omega\sigma \gg 1$, Eq. (18) represents a multicycle (mc) pulse. To model the single-cycle (sc) pulses employed in Fig. 2, we evaluate Eq. (18) in the limit $\omega\sigma \lesssim \pi$ and then substitute $\omega \to 2/\sigma$,

$$E(t) = E_0\{2\sin(\varphi)\, t/\sigma + \cos(\varphi)[1 - 2(t/\sigma)^2]\}\, e^{-(t/\sigma)^2}. \tag{19}$$

The substitution ensures that the peak values of the mc versus sc pulses match, so that the comparison of both is meaningful.

We evaluate the shape functional, given by Eq. (16), for the mc and sc pulses, given by Eqs. (18) and (19), and obtain

$$\mathcal{F}[s] = \sigma^2 \sin(\varphi) \begin{cases} \frac{2\sqrt{\pi}}{3\sqrt{3}} & \text{for sc pulses} \\ \frac{e^{-(\omega\sigma)^2/12}}{4\sqrt{3/\pi}\,\omega\sigma} & \text{for mc pulses.} \end{cases} \tag{20}$$

As seen here, mc pulses are exponentially suppressed as compared to sc pulses. Further, largest remnant currents are produced at a CEP $\varphi = \pi/2$.

*Numerics.* Figure 5 shows numerically calculated remnant currents and confirms the analytical predictions made for the limit of small field strengths: (i) As guided by the black dashed line, we observe a cubic $E_0$ dependence of remnant currents for all shapes in the small field strength limit. (ii) The sc

pulses produce remnant currents exceeding the ones of mc pulses by orders of magnitude. (iii) To compare the effect of different pulse lengths, we keep the number of half cycles, i.e., $\omega\sigma$, invariant, while scaling $\sigma$. In this procedure, reducing the pulse duration by one order of magnitude reduces the remnant current in Fig. 5(a) by two orders of magnitude, as predicted by the $\sigma^2$ dependence in Eq. (20). (iv) For pulses with a CEP of $\varphi = 0$, the remnant current strength is suppressed. Taking Eq. (20) at face value implies the absence of remnant currents; nonzero values observed in Fig. 5(b) reflects terms of $O(\omega/\gamma)$ that have been ignored when deriving Eq. (20). (v) Exploring higher field strengths, we find that the predictions made from analyzing the leading terms still hold in this regime: here, too, sc pulses with a CEP of $\varphi = \pi/2$ lead to the largest remnant currents out of all considered shapes.

*Relation to experiments.* In experiments about remnant currents, pulse configurations comparable to the red trace in the inset of Fig. 5(a) have been used [33–35]. According to Eq. (20) and Fig. 5, the remnant currents' strength can be increased by up to five orders of magnitude as compared to the experimental findings by employing single-cycle pulses instead of multicycle pulses while keeping the peak field strength constant.

## VI. MATERIALS: REMNANT CURRENTS IN TOPOLOGICAL SURFACE STATES AND TMDCs

For the case of a massive Dirac Hamiltonian, given by Eq. (7), we obtain a closed expression for the material constant $C := C(\tilde{\epsilon}_\mathrm{F}, \tilde{m}_z)$, with $\tilde{\epsilon}_\mathrm{F} := \epsilon_\mathrm{F}/\gamma$ and $\tilde{m}_z := m_z/\gamma$. The full analytical expression of $C$ is shown in Eq. (C1) in Appendix C.

The limiting case of zero mass $m_z = 0$ and $\tilde{\epsilon}_\mathrm{F} \gg 1$ may serve to model a gapless topological surface state (TSS) [76] and the material constant reads

$$C^\mathrm{TSS} = \frac{q^4 v_\mathrm{F}^2}{32\gamma^2\tilde{\epsilon}_\mathrm{F}^3} + O\big(\tilde{\epsilon}_\mathrm{F}^{-4}\big). \tag{21}$$

Note that $C^\mathrm{TSS}$ diverges for $\tilde{\epsilon}_\mathrm{F} = 0$, signalizing a breakdown of the perturbative expansion.

Another limit, $\tilde{m}_z \gg 1$ and $\tilde{\epsilon}_\mathrm{F} = 0$ [77], models a monolayer transition-metal dichalcogenide (TMDC) [67]. We obtain

$$C^\mathrm{TMDC} = \frac{q^4 v_\mathrm{F}^2}{35\gamma^2\tilde{m}_z^3} + O\big(\tilde{m}_z^{-4}\big). \tag{22}$$

To compare these materials, we consider the fraction

$$\frac{\hat{j}_\parallel^{(\infty)}(\mathrm{TSS})}{\hat{j}_\parallel^{(\infty)}(\mathrm{TMDC})} = \frac{C^\mathrm{TSS}}{C^\mathrm{TMDC}} \approx \frac{m_z^3}{\epsilon_\mathrm{F}^3}, \tag{23}$$

which is independent of the pulse shape. Using typical parameters $\epsilon_\mathrm{F} = 0.2$ eV [76], $\gamma = (10\ \mathrm{fs})^{-1}$ [58], $m_z = 2$ eV [67], and assuming $v_\mathrm{F}$ to be equal in the TSS and the TMDC, we estimate $C^\mathrm{TSS}/C^\mathrm{TMDC} \approx 10^3$. In the case of strong doping, the Fermi level can cut into the conduction band. In this case, Eq. (C1) has to be expanded in the limit of large $\epsilon_\mathrm{F}$ and large $m_z$. The leading terms are the same as in the TSS case, given by Eq. (21); if the Fermi level cuts into the conduction band, $\epsilon_\mathrm{F} \gtrsim m_z$ and thus $C \lesssim C^\mathrm{TMDC}$.

In summary, a TSS (or graphene) is an ideal platform to explore large remnant currents.

## VII. CONCLUSION

In this work, we have performed combined analytical and numerical analyses of steady-state (remnant) currents that continue to flow in a material long after the driving laser pulse has died out. We predict conditions under which remnant currents can be of the same order of magnitude as the transient current under driving. Moreover, remnant currents will be orders of magnitude larger for single-cycle pulses compared to the multicycle pulses that have been used in experimental remnant current studies so far. Our prediction relies on an analytical formula that we have derived. It explains the strong dependence of remnant currents on laser pulse shape and Hamiltonian parameters. We believe that our finding helps to boost potential applications of remnant currents in ultrafast electronics.

For all SBE simulations, we have used our program package CUED, that is freely available from github [78]. All inputs and outputs of CUED used for this work are available on zenodo [79], together with the code version that has been used for generating the inputs and outputs.

## ACKNOWLEDGMENTS

We thank J. Freudenstein, M. Meierhofer, C. Meinecke, and J. Schlosser for helpful discussions. Further, we express our gratitude to P. Hommelhoff for critical reading of our manuscript. Support from the German Research Foundation (DFG) through the Collaborative Research Center, Project ID No. 314695032 SFB 1277 (Project A03), GRK 2907, and further Grants No. EV30/11-2 and No. EV30/12-1 is gratefully acknowledged. J.W. acknowledges funding by the DFG via the Emmy Noether Programme (Project No. 503985532). The authors gratefully acknowledge the scientific support and HPC resources provided by the Erlangen National High Performance Computing Center (NHR@FAU) of the Friedrich-Alexander-Universität Erlangen-Nürnberg (FAU) under the NHR Project No. b165da10. NHR funding is provided by federal and Bavarian state authorities. NHR@FAU hardware is partially funded by the German Research Foundation (DFG), Grant No. 440719683.

## APPENDIX A: NATURAL UNITS OF REMNANT CURRENTS

In all calculations, we have set $\hbar = 1$. The small parameter of the perturbative expansion in the field strengths in Eq. (1) is $\tilde{E}_0 = q\sigma E_0/k_\mathrm{F}$. However, as the pulse duration $\sigma$ is a variable parameter in our analysis, we choose $\epsilon_\mathrm{F}^{-1}$ as the natural timescale of our problem. With the Fermi vector $k_\mathrm{F}$ as the typical length scale of the problem, the natural units to express electric fields is $qE(t)/(k_\mathrm{F}\epsilon_\mathrm{F})$. For the current density, given by Eq. (6), the BZ integral can be compared with the square of the Fermi vector $k_\mathrm{F}^2$ and the derivative of the band energy can be related to $\epsilon_\mathrm{F}/k_\mathrm{F}$. Therefore, a natural way to express the remnant current density is $j^{(\infty)}/(qk_\mathrm{F}\epsilon_\mathrm{F})$.

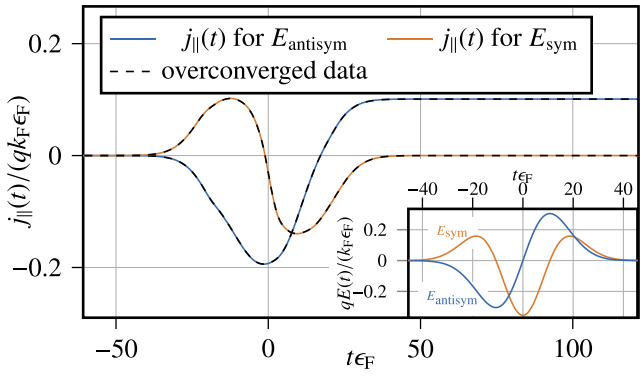


FIG. 6. Convergence check for Fig. 2. Colored lines are the data plotted in the main part with 800 × 144 points, a BZ size of 1.89 × 0.95 Å$^{-1}$, and an integration time step of 0.01 fs. Dashed lines are overconverged data with 1080 × 288 points, a BZ size of 2.27 × 1.13 Å$^{-1}$, and an integration time step of 0.008 fs.

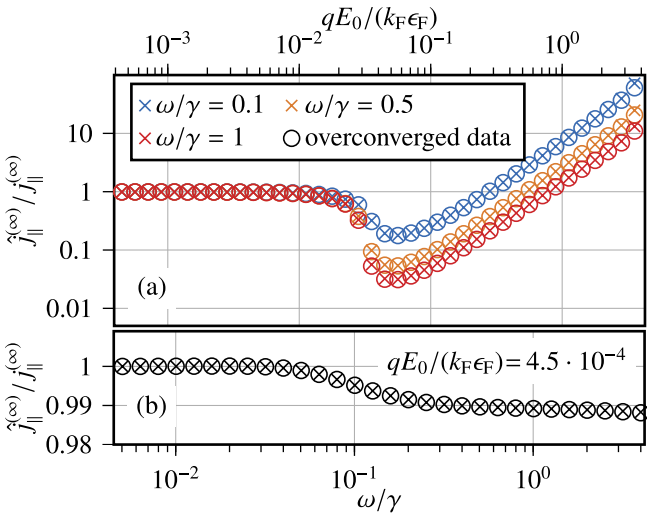


FIG. 7. Convergence check for Fig. 4. Crosses are the data plotted in the main part with 800 × 360 points and a BZ size of 1.89 × 0.95 Å$^{-1}$ for $E_0 \leqslant 1.0$ MV/cm $= 0.71 k_F\epsilon_F/q$, and 2400 × 504 points and a BZ size of 11.34 × 2.65 Å$^{-1}$ for $E_0 > 1.0$ MV/cm $= 0.71 k_F\epsilon_F/q$. The integration time step for all pulses with width 50 fs and CEP $\varphi = 0$ was 0.01 fs, and 0.005 fs for all other pulses. Circles are overconverged with 1200 × 504 points and a BZ size of 2.27 × 1.13 Å$^{-1}$ for $E_0 \leqslant 1.0$ MV/cm $= 0.71 k_F\epsilon_F/q$, and 3000 × 648 points and a BZ size of 13.23 × 3.02 Å$^{-1}$ for $E_0 > 1.0\,\text{MV/cm} = 0.71 k_F\epsilon_F/q$. The integration time step for all pulses with width 50 fs and CEP $\varphi = 0$ was 0.008 fs, and 0.004 fs for all other pulses.

## APPENDIX B: MARKOV REGIME OF SECOND-ORDER OCCUPATION CHANGES

For sufficiently large damping $\gamma$, only times where $t_2$ is close to $t_1$ are contributing to the $t_2$ integral from Eq. (13). This can be seen following the arguments below.

Expanding $w_{ij}(t_2) - w_{ij}(t_1)$ in the exponent for small $\Delta t := t_2 - t_1$ enables us to evaluate the $t_2$ integral in the leading order in $\Delta t$. To do so, we introduce $D(t_1, t_2) := \mathbf{E}(t_1) \cdot \mathbf{d}_{\underline{n}n}(\mathbf{k}_{t_1})\mathbf{E}(t_2) \cdot \mathbf{d}_{n\underline{n}}(\mathbf{k}_{t_2})$ to shorten the notation and expand the exponent around $\Delta t$,

$$\begin{aligned}
&\int_{t_0}^{t} \mathrm{d}t_1 \int_{t_0}^{t_1} \mathrm{d}t_2 e^{(t_2-t_1)\gamma + \mathrm{i}[w(t_2)-w(t_1)]} D(t_1, t_2) \\
&= \int_{t_0}^{t} \mathrm{d}t_1 \int_{t_0-t_1}^{0} \mathrm{d}\Delta t e^{\Delta t\gamma + \mathrm{i}[w(\Delta t+t_1)-w(t_1)] + \ln[D(t_1, \Delta t+t_1)]} \\
&= \int_{t_0}^{t} \mathrm{d}t_1 \int_{t_0-t_1}^{0} \mathrm{d}\Delta t\; e^{\Delta t[\gamma + \mathrm{i}\dot{w}(t_1)] + \frac{1}{2} i\dot{w}(t_1)\Delta t^2} \\
&\quad \times e^{\ln D(t_1,t_1) + \partial_{\Delta t} \ln\left[D(t_1, t_1+\Delta t)_{|\Delta t=0}\right]\Delta t} \\
&\quad \times e^{\frac{1}{2}\partial_{\Delta t}^2 \ln[D(t_1,t_1+\Delta t)]^2_{|\Delta t=0}\Delta t^2 + O(\Delta t^3)}.
\end{aligned} \tag{B1}$$

Introducing

$$\gamma_{\text{eff}}^{(1)}(t_1) := \gamma + \mathrm{i}\dot{w}(t_1) + \partial_{\Delta t} \ln[D(t_1, t_1+\Delta t)_{|\Delta t=0}], \tag{B2}$$

$$\gamma_{\text{eff}}^{(2)}(t_1) := \tfrac{1}{2}\left\{\mathrm{i}\ddot{w}(t_1) + \partial_{\Delta t}^2 \ln[D(t_1, t_1+\Delta t)]^2_{|\Delta t=0}\right\}, \tag{B3}$$

we can write the integral as

$$\begin{aligned}
&\int_{t_0}^{t} \mathrm{d}t_1 \int_{t_0-t_1}^{0} \mathrm{d}\Delta t e^{\gamma_{\text{eff}}^{(1)}(t_1)\Delta t + \gamma_{\text{eff}}^{(2)}\Delta t^2 + O(\Delta t^3)} D(t_1, t_1) \\
&= \int_{t_0}^{t} \mathrm{d}t_1 \frac{1 - e^{(t_0-t_1)\gamma_{\text{eff}}^{(1)}(t_1)}}{\gamma_{\text{eff}}^{(1)}(t_1)} D(t_1, t_1)\left[1 + O\left(\frac{|\gamma_{\text{eff}}^{(2)}|}{|\gamma_{\text{eff}}^{(1)}|^2}\right)\right] \\
&= \int_{t_0}^{t} \mathrm{d}t_1 \frac{D(t_1, t_1)}{\gamma_{\text{eff}}^{(1)}}\left[1 + O\left(\frac{|\gamma_{\text{eff}}^{(2)}|}{|\gamma_{\text{eff}}^{(1)}|^2}\right)\right].
\end{aligned} \tag{B4}$$

For a large $\gamma_{\text{eff}}^{(1)}$, the factor $e^{(t_0-t_1)\gamma_{\text{eff}}^{(1)}(t_1)}$ has a sharp peak around $t_1 = t_0$ and is negligible for $(t_1 - t_0)\gamma_{\text{eff}}^{(1)}(t_1) \gg 1$. $D(t_1, t_1)$ is a function of the electric field pulse, which starts at $t_0$. If we assume a slowly increasing pulse, we have $D \approx 0$ for those times, where the exponential function is not negligible. Thus, if the peaks of $e^{(t_0-t_1)\gamma_{\text{eff}}^{(1)}(t_1)}$ and $D(t_1, t_1)$ are well separated, the integral containing the exponential in Eq. (B4) is negligible compared to the integral of $D(t_1, t_1)/\gamma_{\text{eff}}^{(1)}$, justifying the last step in Eq. (B4). This is the case for all pulses that we consider in the main part of the manuscript. Lastly, we can expand $1/\gamma_{\text{eff}}^{(1)}$ in the limit of large $\gamma$, utilizing that $\partial_t D(t, t) \propto \omega$, which is the typical frequency of the driving field. Keeping only leading terms in $\omega/\gamma$, as terms of $O(|\gamma_{\text{eff}}^{(2)}|/|\gamma_{\text{eff}}^{(1)}|^2)$ are also at least of $O(\omega/\gamma)$, we can simplify the remaining integral by

$$\begin{aligned}
&\int_{t_0}^{t} \mathrm{d}t_1 \frac{D(t_1, t_1)}{\gamma_{\text{eff}}^{(1)}(t_1)}\left[1 + O\left(\frac{|\gamma_{\text{eff}}^{(2)}|}{|\gamma_{\text{eff}}^{(1)}|^2}\right)\right] \\
&= \int_{t_0}^{t} \mathrm{d}t_1 \frac{D(t_1, t_1)}{\gamma + \mathrm{i}\dot{w}(t_1)}[1 + O(\omega/\gamma)].
\end{aligned} \tag{B5}$$

Reinserting the definition of $D(t_1, t_2)$ and $\dot{w}(t_1) = \epsilon(\mathbf{k}_{t_1})$ then leads to Eq. (14) in the main part of the manuscript. In the case of zero off-diagonal damping ($\gamma = 0$), we cannot perform the simplifications done in the last step and have to use $\gamma_{\text{eff}}^{(1)}(t_1)$ to approximate the density matrix elements. In this work, however, we will always assume nonzero damping, $\gamma > 0$.

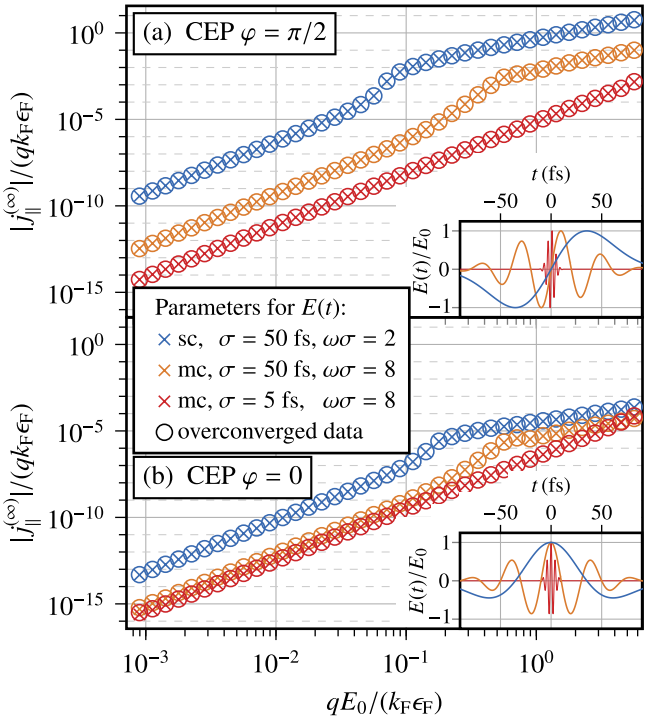


FIG. 8. Convergence check for Fig. 5. Crosses are the data plotted in the main part; circles are the overconverged data. The convergence parameters are the same as in Fig. 7.

## APPENDIX C: MATERIAL-DEPENDENT CONSTANT FOR DIRAC HAMILTONIANS

In this section, we evaluate the material-dependent constant $C$ from Eq. (15) for a massive Dirac cone Hamiltonian from Eq. (7). At zero temperature, the initial occupation $\varrho_{cc}(\mathbf{k}, t_0)$ is either 1, if $|\mathbf{k}| \leqslant k_F$, or 0, if $|\mathbf{k}| > k_F$ and $\varrho_{vv}(\mathbf{k}, t_0) = 1$. As all terms in Eq. (15) are proportional to $[\varrho_{vv}(\mathbf{k}, t_0) - \varrho_{cc}(\mathbf{k}, t_0)]$, we can transform the BZ integral into polar coordinates and set the lower limit of the radial integral to $k_F$. Substituting $\tilde{\epsilon}_F := k_F v_F/\gamma$ and $\tilde{m}_z := m_z/\gamma$ and $\zeta := \sqrt{\tilde{\epsilon}_F^2 + \tilde{m}_z^2}$, we obtain a closed expression for $C$:

$$
\begin{aligned}
C(\tilde{\epsilon}_F, \tilde{m}_z) = {} & \frac{q^4 v_F^2}{240\gamma^2\zeta^6(1 + 4\tilde{\epsilon}_F^2 + 4\tilde{m}_z^2)\pi} \\
& \times \Big\{ -64\tilde{m}_z^4 - 76\tilde{m}_z^6 - 2880\tilde{m}_z^{10} \\
& + \big(-160\tilde{m}_z^2 - 356\tilde{m}_z^4 + 480\tilde{m}_z^6 - 8640\tilde{m}_z^8\big)\tilde{\epsilon}_F^2 \\
& + \big(-60 - 460\tilde{m}_z^2 + 960\tilde{m}_z^4 - 8640\tilde{m}_z^6\big)\tilde{\epsilon}_F^4 \\
& + \big(-180 + 480\tilde{m}_z^2 - 2880\tilde{m}_z^4\big)\tilde{\epsilon}_F^6 \\
& + \big(48\tilde{m}_z^4 - 8\tilde{m}_z^2 + 3\big)\zeta^5\big(4\tilde{\epsilon}_F^2 + 4\tilde{m}_z^2 + 1\big) \\
& \times [15\pi - 30\tan^{-1}(2\zeta)]\Big\}. \qquad \text{(C1)}
\end{aligned}
$$

For a gapless Dirac cone, we have

$$
\begin{aligned}
C(\tilde{\epsilon}_F, \tilde{m}_z = 0) = {} & \frac{q^4 v_F^2}{16\gamma^2\tilde{\epsilon}_F(1 + 4\tilde{\epsilon}_F^2)\pi} \\
& \times \big[12\pi\tilde{\epsilon}_F^3 - 12\tilde{\epsilon}_F^2 + 3\pi\tilde{\epsilon}_F - 4 \\
& - 6\big(4\tilde{\epsilon}_F^3 + \tilde{\epsilon}_F\big)\tan^{-1}(2\tilde{\epsilon}_F)\big]. \qquad \text{(C2)}
\end{aligned}
$$

## APPENDIX D: COMPUTATIONAL DETAILS

For the Brillouin zone sampling, we employ Monkhorst-Pack meshes [80]. We carefully checked convergence of the Monkhorst-Pack mesh, reaching converged results for meshes with a density of up to 322 500 $k$ points per Å$^{-2}$ and BZ sizes of up to $11.34 \times 2.65$ Å$^{-1}$. Time integration is performed using a fourth-order Runge-Kutta solver with time steps of at least 0.005 fs. We show in Figs. 6–8 that increasing the BZ size and $k$-point density, and decreasing the time step of the integration, do not change the values of our calculations

We employ an electric field that is linearly polarized in the $x$ direction. Unless otherwise stated, we employ a gapless Dirac cone with an equilibrium band occupation of a Fermi-Dirac distribution with an Fermi level of 0.2 eV at zero temperature. The off-diagonal dephasing rate $\gamma$ for all plots besides Fig. 4 is chosen to be $10^{-1}$ fs [58].


[1] F. Krausz and M. I. Stockman, Attosecond metrology: From electron capture to future signal processing, Nat. Photon. **8**, 205 (2014).

[2] O. Schubert, M. Hohenleutner, F. Langer, B. Urbanek, C. Lange, U. Huttner, D. Golde, T. Meier, M. Kira, S. W. Koch *et al.*, Sub-cycle control of terahertz high-harmonic generation by dynamical Bloch oscillations, Nat. Photon. **8**, 119 (2014).

[3] T. Kampfrath, K. Tanaka, and K. A. Nelson, Resonant and nonresonant control over matter and light by intense terahertz transients, Nat. Photon. **7**, 680 (2013).

[4] T. Seifert, S. Jaiswal, U. Martens, J. Hannegan, L. Braun, P. Maldonado, F. Freimuth, A. Kronenberg, J. Henrizi, I. Radu *et al.*, Efficient metallic spintronic emitters of ultrabroadband terahertz radiation, Nat. Photon. **10**, 483 (2016).

[5] C. Meineke, M. Prager, J. Hayes, Q. Wen, L. Z. Kastner, D. Schuh, K. Fritsch, O. Pronin, M. Stein, F. Schäfer *et al.*, Scalable high-repetition-rate sub-half-cycle terahertz pulses from spatially indirect interband transitions, Light Sci. Appl. **11**, 151 (2022).

[6] M. Meierhofer, S. Maier, D. Afanasiev, J. Freudenstein, J. Riepl, J. Helml, C. P. Schmid, and R. Huber, Interferometric carrier-envelope phase stabilization for ultrashort pulses in the mid-infrared, Opt. Lett. **48**, 1112 (2023).

[7] A. H. Chin, O. G. Calderón, and J. Kono, Extreme midinfrared nonlinear optics in semiconductors, Phys. Rev. Lett. **86**, 3292 (2001).

[8] S. Ghimire, A. D. DiChiara, E. Sistrunk, P. Agostini, L. F. DiMauro, and D. A. Reis, Observation of high-order harmonic generation in a bulk crystal, Nat. Phys. **7**, 138 (2011).

[9] M. Hohenleutner, F. Langer, O. Schubert, M. Knorr, U. Huttner, S. W. Koch, M. Kira, and R. Huber, Real-time observation of interfering crystal electrons in high-harmonic generation, Nature (London) **523**, 572 (2015).

[10] G. Vampa, C. R. McDonald, G. Orlando, D. D. Klug, P. B. Corkum, and T. Brabec, Theoretical analysis of high-

harmonic generation in solids, Phys. Rev. Lett. **113**, 073901 (2014).
[11] R. Silva, Á. Jiménez-Galán, B. Amorim, O. Smirnova, and M. Ivanov, Topological strong-field physics on sub-laser-cycle timescale, Nat. Photon. **13**, 849 (2019).
[12] C. P. Schmid, L. Weigl, P. Grössing, V. Junk, C. Gorini, S. Schlauderer, S. Ito, M. Meierhofer, N. Hofmann, D. Afanasiev *et al.*, Tunable non-integer high-harmonic generation in a topological insulator, Nature (London) **593**, 385 (2021).
[13] E. Goulielmakis and T. Brabec, High harmonic generation in condensed matter, Nat. Photon. **16**, 411 (2022).
[14] A. J. Uzan-Narovlansky, Á. Jiménez-Galán, G. Orenstein, R. E. F. Silva, T. Arusi-Parpar, S. Shames, B. D. Bruner, B. Yan, O. Smirnova, M. Ivanov *et al.*, Observation of light-driven band structure via multiband high-harmonic spectroscopy, Nat. Photon. **16**, 428 (2022).
[15] M. Graml, M. Nitsch, A. Seith, F. Evers, and J. Wilhelm, Influence of chirp and carrier-envelope phase on noninteger high-harmonic generation, Phys. Rev. B **107**, 054305 (2023).
[16] T. T. Luu, M. Garg, S. Y. Kruchinin, A. Moulet, M. T. Hassan, and E. Goulielmakis, Extreme ultraviolet high-harmonic spectroscopy of solids, Nature (London) **521**, 498 (2015).
[17] M. Borsch, C. P. Schmid, L. Weigl, S. Schlauderer, N. Hofmann, C. Lange, J. T. Steiner, S. W. Koch, R. Huber, and M. Kira, Super-resolution lightwave tomography of electronic bands in quantum materials, Science **370**, 1204 (2020).
[18] J. Freudenstein, M. Borsch, M. Meierhofer, D. Afanasiev, C. P. Schmid, F. Sandner, M. Liebich, A. Girnghuber, M. Knorr, M. Kira *et al.*, Attosecond clocking of correlations between Bloch electrons, Nature (London) **610**, 290 (2022).
[19] T. Higuchi, C. Heide, K. Ullmann, H. B. Weber, and P. Hommelhoff, Light-field-driven currents in graphene, Nature (London) **550**, 224 (2017).
[20] J. Reimann, S. Schlauderer, C. P. Schmid, F. Langer, S. Baierl, K. A. Kokh, O. E. Tereshchenko, A. Kimura, C. Lange, J. Güdde *et al.*, Subcycle observation of lightwave-driven dirac currents in a topological surface band, Nature (London) **562**, 396 (2018).
[21] C. Heide, T. Higuchi, H. B. Weber, and P. Hommelhoff, Coherent electron trajectory control in graphene, Phys. Rev. Lett. **121**, 207401 (2018).
[22] C. Lefebvre, D. Gagnon, F. Fillion-Gourdeau, and S. MacLean, Carrier-envelope phase effects in graphene, J. Opt. Soc. Am. B **35**, 958 (2018).
[23] K. F. Mak, K. L. McGill, J. Park, and P. L. McEuen, The valley Hall effect in $mos_2$ transistors, Science **344**, 1489 (2014).
[24] S. A. Oliaei Motlagh, J.-S. Wu, V. Apalkov, and M. I. Stockman, Femtosecond valley polarization and topological resonances in transition metal dichalcogenides, Phys. Rev. B **98**, 081406(R) (2018).
[25] S. A. O. Motlagh, F. Nematollahi, A. Mitra, A. J. Zafar, V. Apalkov, and M. I. Stockman, Ultrafast optical currents in gapped graphene, J. Phys.: Condens. Matter **32**, 065305 (2020).
[26] Á. Jiménez-Galán, R. Silva, O. Smirnova, and M. Ivanov, Lightwave control of topological properties in 2D materials for sub-cycle and non-resonant valley manipulation, Nat. Photon. **14**, 728 (2020).
[27] Álvaro Jiménez-Galán, R. E. F. Silva, O. Smirnova, and M. Ivanov, Sub-cycle valleytronics: Control of valley polarization using few-cycle linearly polarized pulses, Optica **8**, 277 (2021).
[28] T. Rybka, M. Ludwig, M. F. Schmalz, V. Knittel, D. Brida, and A. Leitenstorfer, Sub-cycle optical phase control of nanotunneling in the single-electron regime, Nat. Photon. **10**, 667 (2016).
[29] M. Borsch, M. Meierhofer, R. Huber, and M. Kira, Lightwave electronics in condensed matter, Nat. Rev. Mater. **8**, 668 (2023).
[30] A. Bharti and G. Dixit, Tailoring photocurrent in Weyl semimetals via intense laser irradiation, Phys. Rev. B **108**, L161113 (2023).
[31] A. Bharti and G. Dixit, Photocurrent generation in solids via linearly polarized laser, Phys. Rev. B **109**, 104309 (2024).
[32] K. L. Ishikawa, Electronic response of graphene to an ultrashort intense terahertz radiation pulse, New J. Phys. **15**, 055021 (2013).
[33] C. Heide, T. Boolakee, T. Higuchi, H. B. Weber, and P. Hommelhoff, Interaction of carrier envelope phase-stable laser pulses with graphene: The transition from the weak-field to the strong-field regime, New J. Phys. **21**, 045003 (2019).
[34] C. Heide, T. Boolakee, T. Eckstein, and P. Hommelhoff, Optical current generation in graphene: CEP control vs. $\omega + 2\omega$ control, Nanophotonics **10**, 3701 (2021).
[35] C. Heide, T. Boolakee, T. Higuchi, and P. Hommelhoff, Subcycle temporal evolution of light-induced electron dynamics in hexagonal 2D materials, J. Phys. Photon. **2**, 024004 (2020).
[36] E. Wu, C. Zhang, Z. Wang, and C. Liu, Waveform control of currents in graphene by chirped few-cycle lasers, New J. Phys. **22**, 033016 (2020).
[37] T. Boolakee, C. Heide, A. Garzón-Ramírez, H. B. Weber, I. Franco, and P. Hommelhoff, Light-field control of real and virtual charge carriers, Nature (London) **605**, 251 (2022).
[38] In the semiclassical approximation [41,81–83], the time-dependent current density is given by

$$\mathbf{j}(t) = q \sum_n \int_{\mathrm{BZ}} \frac{\mathrm{d}\mathbf{k}}{(2\pi)^d}\, \mathbf{v}_n(\mathbf{k} - \mathbf{A}(t))\, f_n^{(0)}(\mathbf{k} - \mathbf{A}(t)),$$

$$\times\, \mathbf{v}_n(\mathbf{k}) = \frac{\partial \epsilon_n(\mathbf{k})}{\partial \mathbf{k}} + \mathbf{E}(t) \times \mathbf{\Omega}_n(\mathbf{k}),\ \ \mathbf{A}(t)$$

$$= \int_{-\infty}^{t} \mathbf{E}(\tau) d\tau,$$

where $f_n^{(0)}(\mathbf{k})$ is the initial occupation of band $n$ at crystal momentum $\mathbf{k}$ in the Brillouin zone (BZ) and $\mathbf{\Omega}_n(\mathbf{k})$ is the Berry curvature. For gauge consistency, the vector potential $\mathbf{A}(t)$ (Coulomb gauge) and the electric field vanish for long times (see also [84]), such that we have

$$\lim_{t\to\infty} \mathbf{j}(t) = q \sum_n \int_{\mathrm{BZ}} \frac{\mathrm{d}\mathbf{k}}{(2\pi)^d} \frac{\partial \epsilon_n(\mathbf{k})}{\partial \mathbf{k}} f_n^{(0)}(\mathbf{k}) =: \mathbf{j}^{(0)},$$

where $\mathbf{j}^{(0)}$ denotes the initial current before irradiation implying the absence of remnant currents.
[39] S. Schmitt-Rink, D. S. Chemla, and H. Haug, Nonequilibrium theory of the optical Stark effect and spectral hole burning in semiconductors, Phys. Rev. B **37**, 941 (1988).
[40] M. Lindberg and S. W. Koch, Effective Bloch equations for semiconductors, Phys. Rev. B **38**, 3342 (1988).
[41] C. Aversa and J. E. Sipe, Nonlinear optical susceptibilities of semiconductors: Results with a length-gauge analysis, Phys. Rev. B **52**, 14636 (1995).
[42] W. Schäfer and M. Wegener, *Semiconductor Optics and Transport Phenomena* (Springer, Heidelberg, 2002).

[43] H. Haug and A.-P. Jauho, *Quantum Kinetics in Transport and Optics of Semiconductors* (Springer, Heidelberg, 2008).

[44] H. Haug and S. W. Koch, *Quantum Theory of the Optical and Electronic Properties of Semiconductors* (World Scientific, New York, 2009).

[45] M. Kira and S. W. Koch, *Semiconductor Quantum Optics* (Cambridge University Press, New York, 2011).

[46] S. Y. Kruchinin, M. Korbman, and V. S. Yakovlev, Theory of strong-field injection and control of photocurrent in dielectrics and wide band gap semiconductors, Phys. Rev. B **87**, 115201 (2013).

[47] I. Al-Naib, J. E. Sipe, and M. M. Dignam, High harmonic generation in undoped graphene: Interplay of inter- and intraband dynamics, Phys. Rev. B **90**, 245423 (2014).

[48] M. Wu, S. Ghimire, D. A. Reis, K. J. Schafer, and M. B. Gaarde, High-harmonic generation from Bloch electrons in solids, Phys. Rev. A **91**, 043839 (2015).

[49] M. S. Wismer, S. Y. Kruchinin, M. Ciappina, M. I. Stockman, and V. S. Yakovlev, Strong-field resonant dynamics in semiconductors, Phys. Rev. Lett. **116**, 197401 (2016).

[50] J. Li, X. Zhang, S. Fu, Y. Feng, B. Hu, and H. Du, Phase invariance of the semiconductor Bloch equations, Phys. Rev. A **100**, 043404 (2019).

[51] X. Zhang, J. Li, Z. Zhou, S. Yue, H. Du, L. Fu, and H.-G. Luo, Ellipticity dependence transition induced by dynamical Bloch oscillations, Phys. Rev. B **99**, 014304 (2019).

[52] J. Wilhelm, P. Grössing, A. Seith, J. Crewse, M. Nitsch, L. Weigl, C. Schmid, and F. Evers, Semiconductor Bloch-equations formalism: Derivation and application to high-harmonic generation from Dirac fermions, Phys. Rev. B **103**, 125419 (2021).

[53] L. Yue and M. B. Gaarde, Structure gauges and laser gauges for the semiconductor Bloch equations in high-order harmonic generation in solids, Phys. Rev. A **101**, 053411 (2020).

[54] L. Yue and M. B. Gaarde, Introduction to theory of high-harmonic generation in solids: Tutorial, J. Opt. Soc. Am. B **39**, 535 (2022).

[55] T. S. Seifert, L. Cheng, Z. Wei, T. Kampfrath, and J. Qi, Spintronic sources of ultrashort terahertz electromagnetic pulses, Appl. Phys. Lett. **120**, 180401 (2022).

[56] P.-K. Lu, A. de Jesus Fernandez Olvera, D. Turan, T. S. Seifert, N. T. Yardimci, T. Kampfrath, S. Preu, and M. Jarrahi, Ultrafast carrier dynamics in terahertz photoconductors and photomixers: Beyond short-carrier-lifetime semiconductors, Nanophotonics **11**, 2661 (2022).

[57] M. Kira and S. W. Koch, Many-body correlations and excitonic effects in semiconductor spectroscopy, Prog. Quantum Electron. **30**, 155 (2006).

[58] I. Floss, C. Lemell, G. Wachter, V. Smejkal, S. A. Sato, X.-M. Tong, K. Yabana, and J. Burgdörfer, *Ab initio* multiscale simulation of high-order harmonic generation in solids, Phys. Rev. A **97**, 011401(R) (2018).

[59] V. Korolev, T. Lettau, V. Krishna, A. Croy, M. Zuerch, C. Spielmann, M. Waechtler, U. Peschel, S. Graefe, G. Soavi, and D. Kartashov, Unveiling the role of electron-phonon scattering in dephasing high-order harmonics in solids, arXiv:2401.129290.

[60] K. Hornberger, Introduction to decoherence theory, in *Entanglement and Decoherence: Foundations and Modern Trends* (Springer, Berlin, Heidelberg, 2009), pp. 221–276.

[61] F. Langer, M. Hohenleutner, C. P. Schmid, C. Poellmann, P. Nagler, T. Korn, C. Schüller, M. S. Sherwin, U. Huttner, J. T. Steiner *et al.*, Lightwave-driven quasiparticle collisions on a subcycle timescale, Nature (London) **533**, 225 (2016).

[62] E. Perfetto and G. Stefanucci, Real-time GW-Ehrenfest-Fan-Migdal method for nonequilibrium 2D materials, Nano Lett. **23**, 7029 (2023).

[63] D. Baykusheva, A. Chacón, D. Kim, D. E. Kim, D. A. Reis, and S. Ghimire, Strong-field physics in three-dimensional topological insulators, Phys. Rev. A **103**, 023101 (2021).

[64] I. Kilen, M. Kolesik, J. Hader, J. V. Moloney, U. Huttner, M. K. Hagen, and S. W. Koch, Propagation induced dephasing in semiconductor high-harmonic generation, Phys. Rev. Lett. **125**, 083901 (2020).

[65] K. Kuroda, J. Reimann, J. Güdde, and U. Höfer, Generation of transient photocurrents in the topological surface state of $Sb_2Te_3$ by direct optical excitation with midinfrared pulses, Phys. Rev. Lett. **116**, 076801 (2016).

[66] A. H. Castro Neto, F. Guinea, N. M. R. Peres, K. S. Novoselov, and A. K. Geim, The electronic properties of graphene, Rev. Mod. Phys. **81**, 109 (2009).

[67] A. Kormanyos, G. Burkard, M. Gmitra, J. Fabian, V. Zolyomi, N. D. Drummond, and V. Falko, $\mathbf{k}\cdot\mathbf{p}$ theory for two-dimensional transition metal dichalcogenide semiconductors, 2D Mater. **2**, 022001 (2015).

[68] C.-X. Liu, X.-L. Qi, H. J. Zhang, X. Dai, Z. Fang, and S.-C. Zhang, Model Hamiltonian for topological insulators, Phys. Rev. B **82**, 045122 (2010).

[69] A gapless Dirac Hamiltonian is time-reversal symmetric and thus features no perpendicular currents, which would break time-reversal symmetry. Introducing a time-reversal breaking term, such as a gap, in turn would produce nonzero currents perpendicular to the driving field.

[70] Experimental measurements of the CEP dependence exhibit a sign change of remnant currents under electric field inversion [34,35,37], indicating that the symmetric situation we consider is indeed experimentally realized.

[71] E. J. Mele, P. Král, and D. Tománek, Coherent control of photocurrents in graphene and carbon nanotubes, Phys. Rev. B **61**, 7669 (2000).

[72] J.-L. Cheng, N. Vermeulen, and J. E. Sipe, Third order optical nonlinearity of graphene, New J. Phys. **16**, 053014 (2014).

[73] S. A. Mikhailov, Quantum theory of the third-order nonlinear electrodynamic effects of graphene, Phys. Rev. B **93**, 085403 (2016).

[74] In our previous work [12,15,52], we use a sine instead of a cosine. Here, we choose the cosine in order to be consistent with the existing literature about residual currents. To compare with our previous publications, one has to transform $\varphi \to \varphi - \pi/2$.

[75] The FWHM is given by $2\sigma\sqrt{\ln 2}$.

[76] Y. L. Chen, J. G. Analytis, J.-H. Chu, Z. K. Liu, S.-K. Mo, X. L. Qi, H. J. Zhang, D. H. Lu, X. Dai, Z. Fang *et al.*, Experimental realization of a three-dimensional topological insulator, $Bi_2Te_3$, Science **325**, 178 (2009).

[77] For a Fermi level in the gap, $k_F = 0$. Thus, we evaluate $C$ at $\tilde{\epsilon}_F = 0$.

[78] https://github.com/ccmt-regensburg/CUED

[79] https://doi.org/10.5281/zenodo.14002355

[80] H. J. Monkhorst and J. D. Pack, Special points for Brillouin-zone integrations, Phys. Rev. B **13**, 5188 (1976).

[81] D. Xiao, M.-C. Chang, and Q. Niu, Berry phase effects on electronic properties, Rev. Mod. Phys. **82**, 1959 (2010).

[82] J. P. Davis and P. Pechukas, Nonadiabatic transitions induced by a time-dependent Hamiltonian in the semiclassical/adiabatic limit: The two-state case, J. Chem. Phys. **64**, 3129 (1976).

[83] M.-C. Chang and Q. Niu, Berry phase, hyperorbits, and the Hofstadter spectrum: Semiclassical dynamics in magnetic Bloch bands, Phys. Rev. B **53**, 7010 (1996).

[84] J. Rauch and G. Mourou, The time integrated far field for Maxwell's and d'Alembert's equations, Proc. Am. Math. Soc. **134**, 851 (2006).